Ultrasonics 91 (2019) 121–128

Contents lists available at ScienceDirect

Ultrasonics

journal homepage: www.elsevier.com/locate/ultras

Study on effect of laser-induced ablation for Lamb waves in a thin plate

Sang Eon Lee[a], Peipei Liu[a], Young Woo Ko[b], Hoon Sohn[a], Byeongjin Park[c], Jung-Wuk Hong[a,*]

[a] Department of Civil and Environmental Engineering, Korea Advanced Institute of Science and Technology, 291 Deahak-ro, Yuseong-gu, Daejeon, 34141, Republic of Korea

[b] Samsung C&T Corporation, 26, Sangil-ro 6-gil, Gangdong-gu, Seoul, 05288, Republic of Korea

[c] Composite Research Division, Korea Institute of Materials Science, 797 Changwondaero, Seongsan-gu, Changwon, Gyeongnam, 51508, Republic of Korea

ARTICLE INFO

Keywords:
Laser ultrasound
Lamb wave
Ablation
LS-Dyna

ABSTRACT

In this paper, the effect of ablation on the shape of elastic waves generated by laser excitation is studied numerically and experimentally. Laser-induced ultrasound has been widely used in the nondestructive testing (NDT) field because it has the advantage that the sensor does not have to be directly attached to the target structure. In the safety assessment process, low energy excitation is used, and thus the structure is not damaged. Most studies related to laser ultrasound have focused on the method of detecting cracks within the elastic range, and there have been few studies on the effect of ablation. This research consists of experiments and numerical analyses. In experiments, elastic waves were generated in an aluminum plate by projecting laser pulses with different energy intensities. The velocities in the thickness direction were measured using a Laser Doppler Velocimeter (LDV) at a point 135 mm away from the excitation point.

In the numerical study, two numerical simulations were carried out using heat flux and normal stress input to mimic laser pulse excitation. A thermo-mechanical simulation by heat flux was conducted to simulate thermal expansion by the laser pulse, and the normal stress was applied to reflect the effect of radiation pressure by ablation, respectively. Waveforms were synthesized by using different magnitude ratios of the obtained numerical responses and were compared with the experiment results. It is found that the effect of radiation pressure should not be neglected if the energy intensity is large although the effect of radiation pressure decreases as the energy intensity decreases. At the energy intensity with which ablation occurs, the effects of thermal expansion and radiation pressure exist simultaneously, and the contribution to the response depends on the energy intensity.

1. Introduction

For the diagnosis of structural safety, high-energy radiation, ultrasound, eddy currents, and magnetic particles methods have been widely used [1]. Non-destructive evaluation method using ultrasonic waves consists of linear methods using reflection and refraction of the waves and nonlinear methods using the interaction of cracks [2]. Among those methods, a laser-induced ultrasonic technique has an advantage for high temperature or hazardous structural safety inspection because the sensor does not need to be directly attached to the structures [3]. A laser-induced guided wave has been utilized for the purpose of non-destructive testing (NDT) [4,5] for several decades. Burrows et al. used Lamb waves generated by a laser for NDT [6]. Dewhurst et al. performed experiments with a cylindrical specimen by applying an unfocused laser beam and measured the surface displacement on the opposite side of the excitation surface using a capacitance transducer. A theoretical model considering both the effects of thermoelastic and normal force shows good agreement with experiment results [7].

Aussel et al. applied a laser pulse to a half of a cylindrical specimen, and measured the surface displacement by changing the measurement position. As a result, the ablation effect was dominant as it was closer to the normal to the point of impact, and the effect of the thermoelastic condition increases as the distance increases [8]. Murray and Wagner compared the theoretical model with the experimental results by superposing the waves generated by the vaporization pressure in the ablative regime and thermoelastic wave effect [9]. Guo et al. applied oblique line-shaped force with a laser to the specimen, and they confirmed that the shear wave is enhanced obviously as shear force increases making the surface wave enhanced in the direction of transverse power flow [10]. Pierce et al. diagnosed a composite material using an ND: YAG laser [11]. Li et al. simulated guided waves generated on the human skin by a laser pulse using FEM [12]. Liao et al. performed the

* Corresponding author.
E-mail addresses: j.hong@kaist.ac.kr, jwhong@alum.mit.edu (J.-W. Hong).

https://doi.org/10.1016/j.ultras.2018.07.019
Received 11 October 2017; Received in revised form 4 June 2018; Accepted 27 July 2018
Available online 29 July 2018
0041-624X/

numerical analysis with the axis-symmetric two-dimensional model to simulate a thin copper film using the Comsol Multiphysics finite element program [13].

Lee et al. performed structural health monitoring of pipelines in a nuclear power plant with guided laser ultrasound [14]. Also, Lee et al. measured mechanical impedance and detected damage using laser ultrasound [15]. Liu and Hong simulated Lamb wave generated by a laser pulse with the subregioning scheme to reduce the computational cost [16]. White et al. performed wavelet-transformation of multiple ultrasonic echoes and applied the separable nonlinear least square method to estimate the associated unknown parameters [17]. Despite this body of work, most studies have focused on PZT-induced wave and crack detection techniques, and fundamental research on laser-induced waves is still needed. To analyze the laser-induced wave accurately, it is required to clarify the excitation conditions. Shi assumed that the major excitation by the laser as exert normal stress on the surface of the structure and presented the analytical and experiment results [18]. The normal force is generated by the radiation pressure due to momentum change and ablation of the photons [19]. On the other hand, Lee described laser excitation as radial traction from the thermal expansion because the heat flux by the laser strike changes the surface temperature abruptly and accompanies the thermal expansion [20]. It is understood that laser excitation would generate both the radiation pressure and the thermal expansion although the ratio of those might vary according to the laser intensity. We perform laser-induced excitation tests and carry out numerical simulations to generate separate responses by the radiation pressure and the thermal expansion, respectively. Then we inversely calculate the contribution from those excitations by analyzing the experiment results.

In Section 2, analytical models for laser-induced waves and their limitations are summarized. In Section 3, experimental conditions and results are presented. In Section 4, the numerical model, simulation conditions, and results are presented and discussed. In Section 5, the experimental and numerical analysis results are compared. The ratios of influences by the radiation pressure and thermal expansion are compared. It is found that the effect of normal stress due to radiation pressure becomes more dominant as the laser intensity increases.

2. Theoretical model of laser-induced wave

Shi et al. considered the major excitation source of the laser-induced wave as the radiation pressure due to the momentum change of photons [18], whereas Lee explained that the radial stress due to thermal expansion is dominant in generating stress waves [20]. In this section, we summarize the analytical models for the laser-induced wave and explain the limitations of the approaches.

2.1. Analytical model by the radial pressure and thermal expansion

An analytical solution of a three-dimensional circularly crested wave was derived in the cylindrical coordinate system to utilize axisymmetric conditions as shown in Fig. 1. The stress boundary due to normal traction from the radial pressure is expressed as

$$\sigma_{zz}(r,t)=\begin{cases} f(r,t) & \text{at } z=+h \\ 0 & \text{at } z=-h \end{cases}, \tag{1}$$

$$\sigma_{zr}(r,t)=0 \quad \text{at } z=\pm h. \tag{2}$$

where σ_{zz} is the normal traction, σ_{zr} is the tangential traction, $f(r,t)$ is the excitation function of the circular source, r is the radius of the laser, and h is half of plate thickness.

Similarly, the stress boundary due to radial traction by the thermal expansion is written as

$$\sigma_{zr}(r,t)=\begin{cases} f(r,t) & \text{at } z=+h \\ 0 & \text{at } z=-h \end{cases}, \tag{3}$$

$$\sigma_{zz}(r,t)=0 \quad \text{at } z=\pm h. \tag{4}$$

In the analytical derivations, it is assumed that there exists only normal stress or radial stress on the top surface of the plate.

2.2. Analytical calculation of guided wave in an infinite plate

Fig. 2 shows the process for solving a nonhomogeneous wave equation. The Fourier-Hankel transform is taken to transform the equation of motion in the cylindrical coordinate system into the frequency-wavenumber domain. Next, the boundary condition is applied to the obtained ordinary differential equation. The time domain solution is derived by taking the inverse Fourier-Hankel transformation of the frequency domain response.

First, the equation of motion is derived from the stress equilibrium equation in the cylindrical coordinate system with the constitutive law as

$$(\lambda+2\mu)\frac{\partial\Delta}{\partial r}+\mu\frac{\partial(\Omega)}{\partial r}=\rho\frac{\partial^2 u_r}{\partial t^2}, \tag{5}$$

$$(\lambda+2\mu)\frac{\partial\Delta}{\partial z}-\frac{\mu}{r}\frac{\partial(r\Omega)}{\partial r}=\rho\frac{\partial^2 u_z}{\partial t^2}, \tag{6}$$

where λ and μ are Lamé constants of the material, u_r and u_z are the displacements in the radial and vertical directions, respectively, and Ω and Δ are defined as

$$\Omega=\frac{\partial u_r}{\partial z}-\frac{\partial u_z}{\partial r}, \tag{7}$$

$$\Delta=\frac{\partial u_r}{\partial r}+\frac{u_r}{r}+\frac{\partial u_z}{\partial_z}. \tag{8}$$

Next, the Fourier-Hankel transform is applied to the displacements as follows:

$$\hat{u}_z(z,k,\omega)=\int_{-\infty}^{\infty}\int_0^{\infty} u_z(z,r,t)rJ_0(kr)e^{j\omega t}\mathrm{d}r\mathrm{d}t, \tag{9}$$

$$\hat{u}_r(z,k,\omega)=\int_{-\infty}^{\infty}\int_0^{\infty} u_r(z,r,t)rJ_1(kr)e^{j\omega t}\mathrm{d}r\mathrm{d}t, \tag{10}$$

where k is the wave number, ω is the frequency, j is imaginary number, $J_0(kr)$ and $J_1(kr)$ are the zeroth and first order Bessel functions, respectively. A set of ordinary differential equations is obtained by substituting the derivatives of displacements into Eqs. (5) and (6) as follows:

$$\mu\frac{\partial^2\hat{u}_r}{\partial z^2}-[(\lambda+\mu)k]\frac{d\hat{u}_z}{dz}+[\rho\omega^2-k^2(\lambda+2\mu)]\hat{u}_r=0, \tag{11}$$

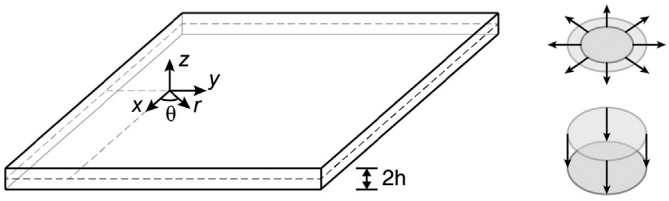

Fig. 1. An analytical model for normal and radial tractions by laser excitation in different directions.

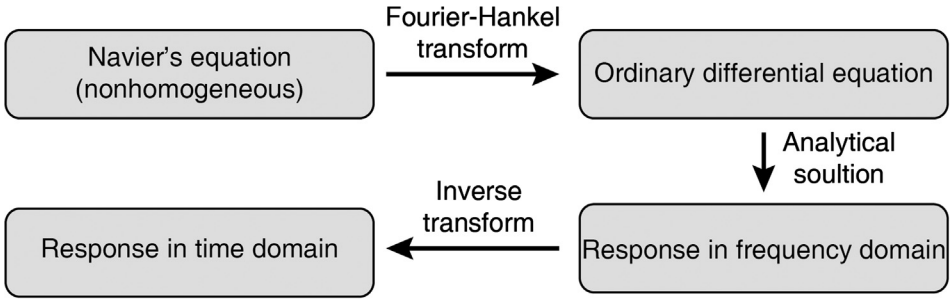

Fig. 2. Flowchart for analytically calculating response in time domain.

$$(\lambda + 2\mu)\frac{\partial^2 \hat{u}_z}{\partial z^2} - [(\lambda + \mu)k]\frac{d\hat{u}_r}{dz} + [\rho\omega^2 - \mu k^2]\hat{u}_z = 0. \tag{12}$$

By considering the displacement field compatibility, the general solutions are written as

$$\hat{u}_r(z, k, \omega) = \{A_s k\cosh(\alpha z) - D_s\beta\cosh(\beta z)\} + \{B_a k\sinh(\alpha z) - C_a\beta\sinh(\beta z)\}, \tag{13}$$

$$\hat{u}_z(z, k, \omega) = -\{A_s\alpha\sinh(\alpha z) - D_s k\sinh(\beta z)\} + \{B_a\alpha\cosh(\alpha z) - C_a k\cosh(\beta z)\}, \tag{14}$$

where A_s, B_a, C_a, and D_s are arbitrary constants, and α and β are defined as

$$\alpha^2 = k^2 - \frac{\omega^2}{c_L^2}, \tag{15}$$

$$\beta = k^2 - \frac{\omega^2}{c_T^2}, \tag{16}$$

where c_L and c_T are the longitudinal and transverse elastic wave velocities, respectively. The arbitrary constants A_s, B_a, C_a, and D_s are calculated by substituting the boundary conditions into Eq. (1)–(4). With the normal traction condition, the coefficients are written by

$$A_s = \frac{-(k^2+\beta^2)\sinh(\beta h)\hat{f}(k,\omega)}{2\mu\{(k^2+\beta^2)^2\cosh(\alpha h)\sinh(\beta h) - 4k^2\alpha\beta\sinh(\alpha h)\cosh(\beta h)\}}, \tag{17}$$

$$B_a = \frac{-(k^2+\beta^2)\cosh(\beta h)\hat{f}(k,\omega)}{2\mu\{(k^2+\beta^2)^2\sinh(\alpha h)\cosh(\beta h) - 4k^2\alpha\beta\cosh(\alpha h)\sinh(\beta h)\}}, \tag{18}$$

$$C_a = \frac{-k\alpha\cosh(\alpha h)\hat{f}(k,\omega)}{\mu\{(k^2+\beta^2)^2\sinh(\alpha h)\cosh(\beta h) - 4k^2\alpha\beta\cosh(\alpha h)\sinh(\beta h)\}}, \tag{19}$$

$$D_s = \frac{-k\alpha\sinh(\alpha h)\hat{f}(k,\omega)}{\mu\{(k^2+\beta^2)^2\cosh(\alpha h)\sinh(\beta h) - 4k^2\alpha\beta\sinh(\alpha h)\cosh(\beta h)\}}. \tag{20}$$

In an analogous manner, the coefficients for the radial traction conditions are obtained as

$$A_s = \frac{-k\beta\cosh(\beta h)\hat{f}(k,\omega)}{\mu\{(k^2+\beta^2)^2\cosh(\alpha h)\sinh(\beta h) - 4k^2\alpha\beta\sinh(\alpha h)\cosh(\beta h)\}}, \tag{21}$$

$$B_a = \frac{-k\beta\sinh(\beta h)\hat{f}(k,\omega)}{\mu\{(k^2+\beta^2)^2\sinh(\alpha h)\cosh(\beta h) - 4k^2\alpha\beta\cosh(\alpha h)\sinh(\beta h)\}}, \tag{22}$$

$$C_a = \frac{-(k^2+\beta^2)\sinh(\alpha h)\hat{f}(k,\omega)}{2\mu\{(k^2+\beta^2)^2\sinh(\alpha h)\cosh(\beta h) - 4k^2\alpha\beta\cosh(\alpha h)\sinh(\beta h)\}}, \tag{23}$$

$$D_s = \frac{-(k^2+\beta^2)\cosh(\alpha h)\hat{f}(k,\omega)}{2\mu\{(k^2+\beta^2)^2\cosh(\alpha h)\sinh(\beta h) - 4k^2\alpha\beta\sinh(\alpha h)\cosh(\beta h)\}}. \tag{24}$$

The stress boundary condition is prescribed as

$$f(r,t) = \frac{1}{2\pi}\int_{-\infty}^{\infty}\int_0^{\infty}\hat{f}(k,\omega)kJ_0(kr)e^{-j\omega t}\mathrm{d}k\mathrm{d}\omega, \tag{25}$$

where $\hat{f}(k,\omega)$ is the Fourier-Hankel transform of the circular source described as

$$\hat{f}(k,\omega) = \frac{rJ_1(kr)}{k}, \tag{26}$$

where r is the radius of the laser beam. The inverse transform pair is then expressed as follows:

$$u_z(z,r,t) = \frac{1}{2\pi}\int_{-\infty}^{\infty}\int_0^{\infty}\hat{u}_z(z,k,\omega)kJ_0(kr)e^{-j\omega t}\mathrm{d}k\mathrm{d}\omega, \tag{27}$$

$$u_r(z,r,t) = \frac{1}{2\pi}\int_{-\infty}^{\infty}\int_0^{\infty}\hat{u}_r(z,k,\omega)kJ_1(kr)e^{-j\omega t}\mathrm{d}k\mathrm{d}\omega. \tag{28}$$

By using the inverse Fourier- Hankel transform, the normal displacements $u_z(z,r,t)$ are expressed as

$$\begin{aligned} u_z(z,r,t) &= \frac{1}{2\pi}\int_{-\infty}^{\infty}\int_0^{\infty}\hat{u}_z(z,k,\omega)kJ_0(kr)e^{-j\omega t}dkd\omega \\ &= \frac{1}{2\pi}\int_{-\infty}^{\infty}\int_0^{\infty}N_z(h,k,\omega)\hat{f}(k,\omega)kJ_0(kr)e^{-j\omega t}dkd\omega \\ &= \frac{1}{4}\int_{-\infty}^{\infty}\sum_k H_z(h,\omega)\hat{f}(k,\omega)kJ_0(kr)e^{-j\omega t}d\omega, \end{aligned} \tag{29}$$

where $N_z(h,k,\omega)$ is the material response, which varies by the traction boundary condition whether normal force or radial force is applied. In the case of normal force excitation, $N_z(h,k,\omega)$ and $H_z(h,\omega)$ are expressed as follows.

$$N_z(h,k,\omega) = \begin{cases} \frac{\alpha(-k^2+\beta^2)\sinh(\alpha h)\sinh(\beta h)}{2\mu\Delta_s} & \text{(symmetric)} \\ \frac{\alpha(-k^2+\beta^2)\cosh(\alpha h)\cosh(\beta h)}{2\mu\Delta_a} & \text{(antisymmetric)} \end{cases}, \tag{30}$$

$$H_z(h,\omega) = \begin{cases} \frac{j\alpha(k^2-\beta^2)\sinh(\alpha h)\sinh(\beta h)}{\mu\Delta_s'} & \text{(symmetric)} \\ \frac{j\alpha(k^2-\beta^2)\cosh(\alpha h)\cosh(\beta h)}{\mu\Delta_a'} & \text{(antisymmetric)} \end{cases}, \tag{31}$$

where Δ_s and Δ_a are determined as follows.

$$\Delta_s = (k^2+\beta^2)^2\cosh(\alpha h)\sinh(\beta h) - 4k^2\alpha\beta\sinh(\alpha h)\cosh(\beta h), \tag{32}$$

$$\Delta_a = (k^2+\beta^2)^2\sinh(\alpha h)\cosh(\beta h) - 4k^2\alpha\beta\cosh(\alpha h)\sinh(\beta h). \tag{33}$$

Here, Δ_s' and Δ_a' represent the derivatives of Δ_s and Δ_a with respect to the wave number k. In Eq. (31), the pole at which the integrand diverges infinitely is located when $\Delta_s = 0$ in the denominator.

On the other hand, with the radial traction boundary condition, $N_z(h,k,\omega)$ is obtained as

$$N_z(h,k,\omega) = \begin{cases} \frac{-k(k^2+\beta^2)\cosh(\alpha h)\sinh(\beta h) + 2k\alpha\beta\sinh(\alpha h)\cosh(\beta h)}{2\mu\Delta_s} & \text{(symmetric)} \\ \frac{-k(k^2+\beta^2)\sinh(\alpha h)\cosh(\beta h) + 2k\alpha\beta\cosh(\alpha h)\sinh(\beta h)}{2\mu\Delta_a} & \text{(antisymmetric)} \end{cases}, \tag{34}$$

$$H_z(h,\omega) = \begin{cases} \frac{j(k^4-\beta^4)\cosh(\alpha h)\sinh(\beta h)}{8k\mu\Delta_s'} & \text{(symmetric)} \\ \frac{j(k^4-\beta^4)\sinh(\alpha h)\cosh(\beta h)}{8k\mu\Delta_a'} & \text{(antisymmetric)} \end{cases}. \tag{35}$$

Setting $\Delta_s = 0$ and $\Delta_a = 0$ in Eqs. (32) and (33) yields the Rayleigh-Lamb frequency equations for symmetric and antisymmetric modes,

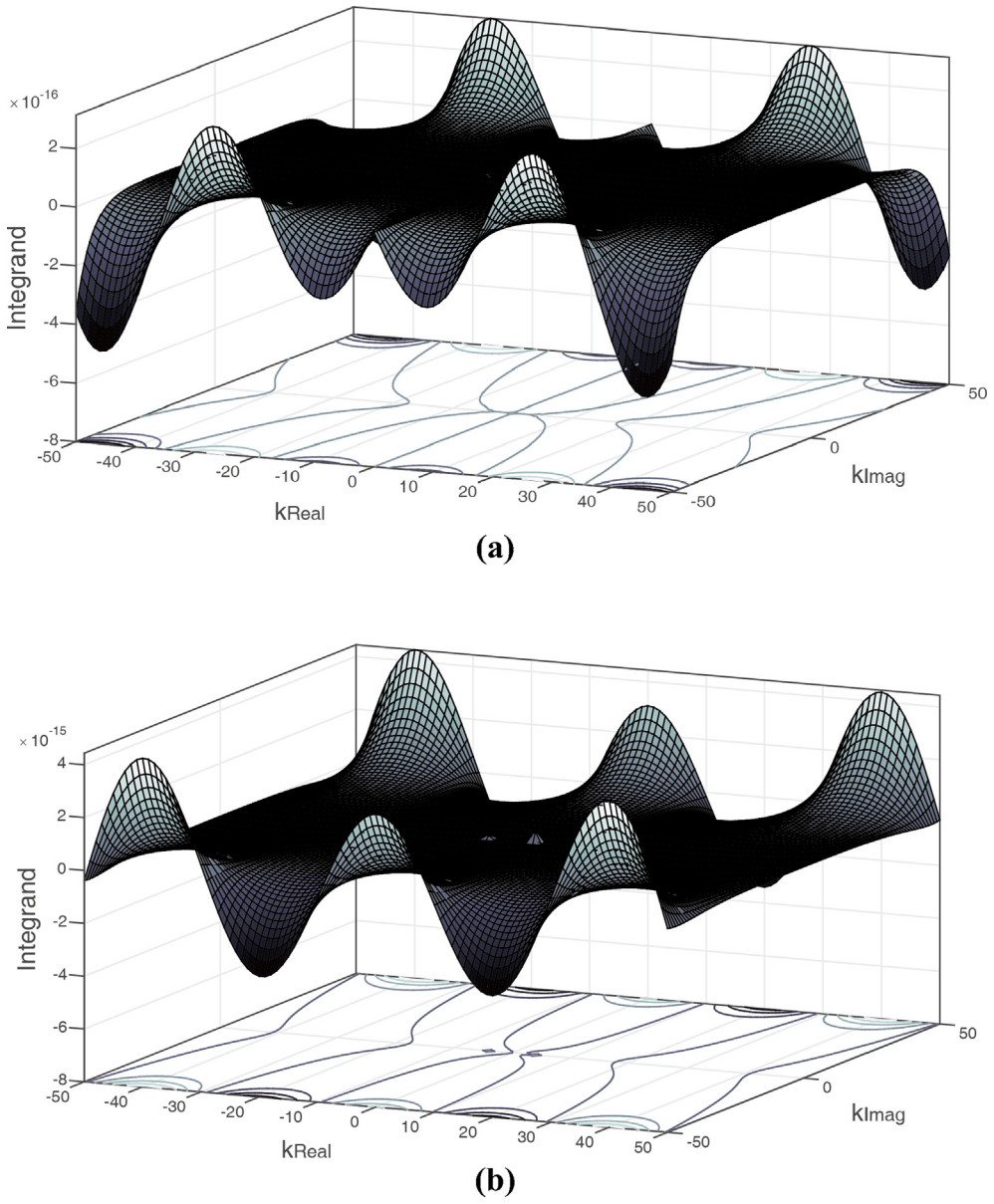

Fig. 3. Integrands of S mode Lamb wave for (a) normal and (b) radial tractions, respectively, in the complex domain.

respectively. The direct integration is not applicable to Eq. (30) because of the existence of poles in the complex domain. Therefore, researchers have utilized the residue theorem to integrate the integrand functions written as

$$\Xi(h, k, \omega, r) = N_z(h, k, \omega)\hat{f}(k, \omega)kJ_0(kr). \tag{36}$$

To apply the residue theorem, an integration path must include the integration from the negative infinity to the positive infinity. However, when the imaginary part of k goes to the positive infinity or the negative infinity, it is observed that the integrands in Eq. (29) diverge due to the existence of the Bessel functions as shown in Fig. 3. The contours in Fig. 3 are plotted by substituting angular velocity ω of 20354 rad/s, laser radius r of 0.25 mm, longitudinal wave speed c_L of 5846.47 m/s, transverse wave speed c_T of 2945.05 m/s, and thickness $2h$ of 3 mm into Eq. (36). The divergence of Bessel functions occurs regardless of excitation direction and Lamb wave mode. The residue theorem cannot be applied to the four combinations of excitation direction and Lamb wave mode. Therefore, we numerically calculate the responses by the normal and radial tractions by using the finite element method (FEM).

3. Experiment results

3.1. Experiment conditions

As shown in Fig. 4, experiments by the laser excitation were carried out on a 3 mm thick plate. The size of the aluminum plate was set to 300 mm × 300 mm so that the incident waveform could be observed before the reflected wave arrives at the target point. The density and Young's modulus of the aluminum 6061-t6 plate to be used in the experiment were measured and summarized in Table 1. The density was calculated by measuring the size and weight of the plate, and the wave speed was measured using a pulse generator by recording the wave arrival time using an oscilloscope. Young's modulus could be calculated from the density and wave speed. Fig. 5 shows that the time domain signal and the magnitude of the wave decreases in propagating through the plate. The longitudinal wave speed was calculated using the time delay information.

An ND: YAG laser was used for excitation, of which the time duration is 12 ns and the maximum energy level is 25 mJ. The diameter of the laser beam varies depending on the focal length and is adjusted to

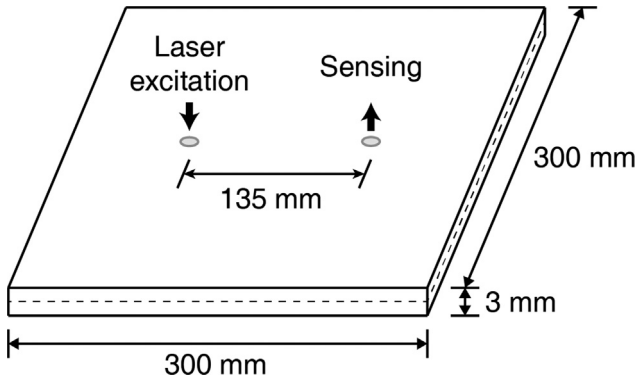

Fig. 4. Schematic of experimental setup. The point of excitation and the point of measurement were set to be symmetric on the square plate.

Table 1
Material properties measured by the experiment.

Material properties	Density	Young's modulus
Aluminum 6061-t6	2738.5 kg/m^3	63.18 GPa

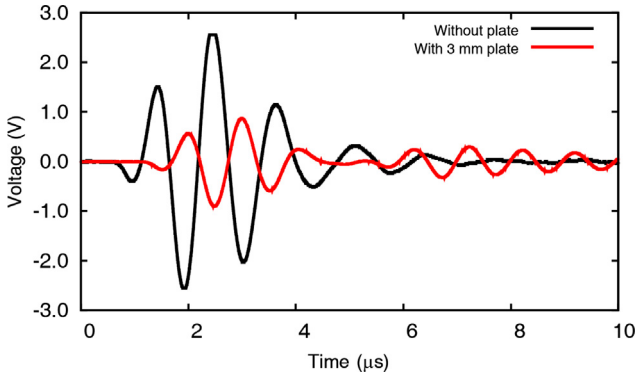

Fig. 5. Time domain signal of p-wave passing through a 3 mm plate compared to the transmitted signal. The wave speed is obtained from the distance and arrival time.

be 0.5 mm. To reduce the disturbance by noise, the excitation and measurement were repeated 1000 times to 5000 times depending on the laser level. The velocity in the normal direction was measured using a laser Doppler velocimeter (LDV). The points of excitation and measurement were arranged symmetrically with respect to the center of the plate, and the distance between two points was 135 mm. The boundary effect was minimized by supporting both ends of the plate with rubber supports.

3.2. Laser-induced Lamb wave

Fig. 6 shows the normalized velocity measured in the thickness direction during the experiments. With relatively weak energy intensities of the laser, the noise was not negligible, but the effect decreases with increasing energy. In Fig. 6(a), it is difficult to accurately measure the arrival time of the longitudinal wave due to the noise, but the arrival time is distinguished clearly in Fig. 6(c) by increasing the laser intensity. The transverse and the surface waves follow the longitudinal wave. By using the waveforms with the increase of the laser intensity, the calculated time delay became more accurate.

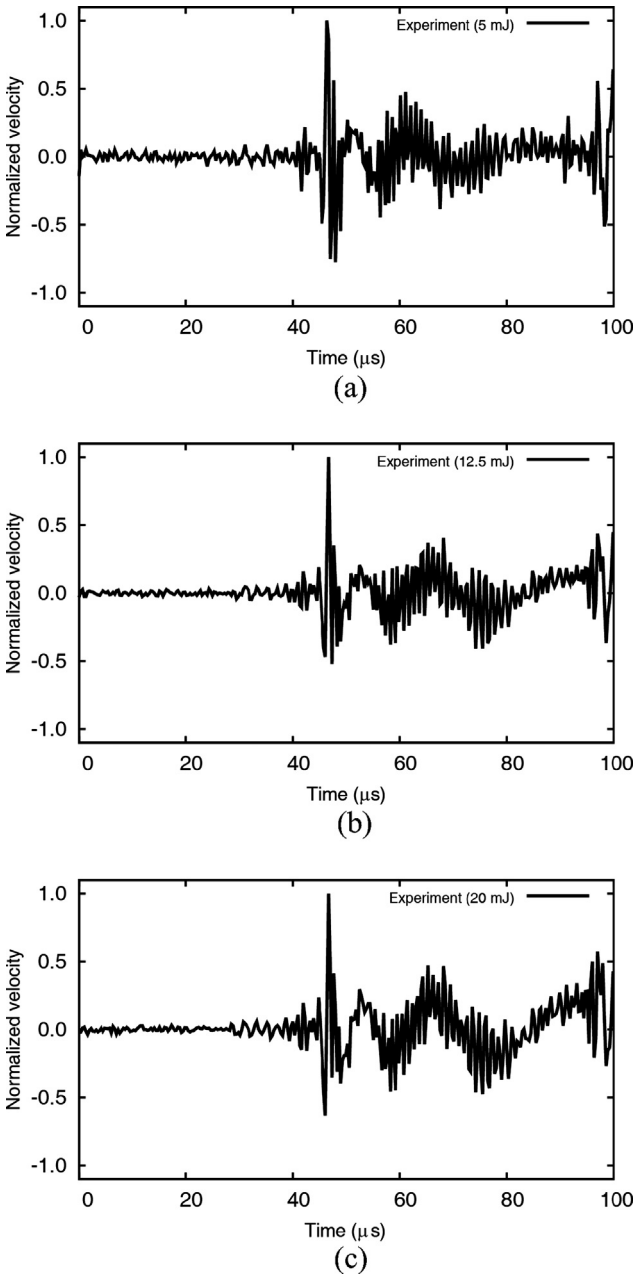

Fig. 6. Velocities measured in the thickness direction at a distance of 135 mm from the point of excitation. The diameter of the laser is 0.5 mm, and the energy levels are (a) 5 mJ, (b) 12.5 mJ, and (c) 20 mJ.

4. Numerical simulations

4.1. Numerical model for thermo-mechanical analysis

A numerical analysis of the laser-induced wave was performed using a commercial FEM software, LS-Dyna [21]. Firstly, the plate was modeled with 8-node brick elements, and the element size was set to 0.5 mm in consideration of the calculation time and wave frequency range. Thus, six elements are arranged in the thickness direction. The thermally excited region by the heat flux from the laser pulse is modeled using smaller elements as shown in Fig. 7(a).

To reduce the calculation time, the symmetric boundary is set as shown in Fig. 7(b), and the plate is fixed in the vertical direction on both sides of the plate considering the experimental conditions. The material properties used in the numerical simulation are summarized in

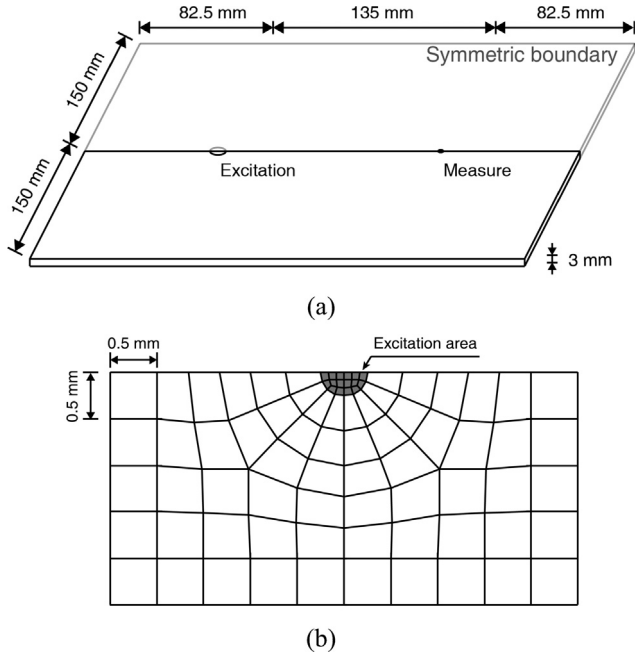

Fig. 7. (a) Schematic of finite element model. A symmetric boundary is used to reduce computation time. (b) An enlarged view of excitation area. The excitation area is modeled using small elements to reflect the circular shape of the laser.

Table 2
Material properties used in the thermoelastic analysis.

Material property (Aluminum 6061-t6)	
Poisson's ratio	0.33
Thermal expansion rate (m/K)	2.2×10^{-5}
Heat capacity (J/kg·K)	896
Thermal conductivity (W/m·K)	167

Table 2. The measured density and Young's modulus from the experiments are used, and thermal properties of the plate are introduced to describe thermo-mechanical response by heat flux.

A specific material model should be used to perform a thermoelastic analysis in the LS-Dyna program. In this study, thermal expansion is implemented in the simulation by using the "Material_Plastic_Elastic" model. Next, the velocity in the thickness direction was measured at a point 135 mm away from the point of excitation.

A numerical analysis is conducted for two types of excitation condition. The first excitation is the heat flux that generates the thermal expansion, and the second is the normal stress corresponding to the radiation pressure. Since the excitation time duration of the ND: YAG laser equipment used in the experiment was 12 ns, the curve of the trapezoidal shape shown in Fig. 8 is used for the numerical simulation. If the time step determined by the element size and material properties is greater than 12 ns, wave propagation is not obtained correctly in the numerical analysis results. Therefore, the initial time step of the analysis should be substantially smaller than 12 ns.

4.2. Simulation results

Fig. 9 shows normalized velocities in the thickness direction obtained from the measuring point shown in Fig. 7(a). Data up to 100 μs are recorded because it is difficult to compare the waveform with the experiment due to the reflected wave after 100 μs. Since there is no influence of noise in the numerical analysis, the velocity remains zero

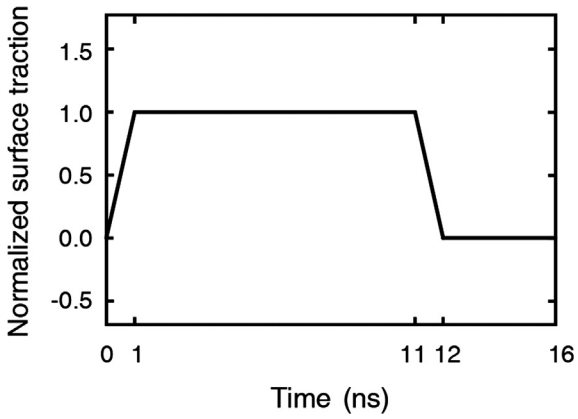

Fig. 8. Temporal profile used for heat flux and normal stress for the duration of 12 ns.

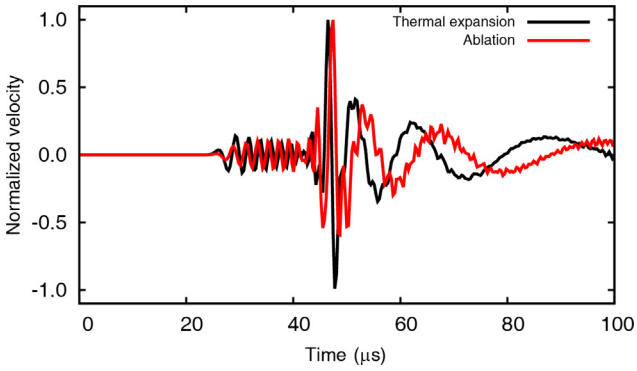

Fig. 9. Normalized velocity in the vertical direction of the plate in numerical simulation. The amplitudes and the arrival times of the waves are different.

until the longitudinal wave arrives. A longitudinal wave with a fast but small amplitude arrives first, followed by a relatively slow transverse wave. When a laser pulse is exerted to a thin plate, a Lamb wave with all modes takes place. Because the velocities of the A_0 mode and the S_0 mode, which have the largest amplitudes among the various modes, are similar to those of the transverse wave, the amplitude of the wave becomes considerably large immediately after the transverse wave arrives. Both numerical results look similar in the waveforms, but it should be noted that there are some differences. Firstly, the longitudinal wave and the transverse wave of two waves reached at 23.1 μs and 45.8 μs, respectively. The wave caused by the thermal expansion has a relatively large negative maximum velocity, whereas the wave caused by the radiation pressure is relatively small. The surface wave by thermal expansion travels slightly slower.

Due to these differences, the waveform differs according to the mixing ratio of the two waves caused by the radiation pressure and thermal expansion in Fig. 9. The results can be used as the basis results to be compared with experiment results for different laser intensities.

4.3. Comparison of numerically simulated results and experiment results

Fig. 6 shows the experimentally measured velocity in the thickness direction on the surface of the aluminum plate. The laser energy level was increased from 5 mJ to 20 mJ by the interval of 2.5 mJ. As the energy level was increased, the surface wave was shifted backward, and the negative velocity which means descending wave tended to decrease. Since the above differences are observed in the numerical results in Section 4, the two waves from the numerical simulations are used as bases to analyze the experiment results shown in Fig. 10.

In Fig. 10, m and n represent the mixing ratio of the wave by thermal expansion and radiation pressure. Using the least square

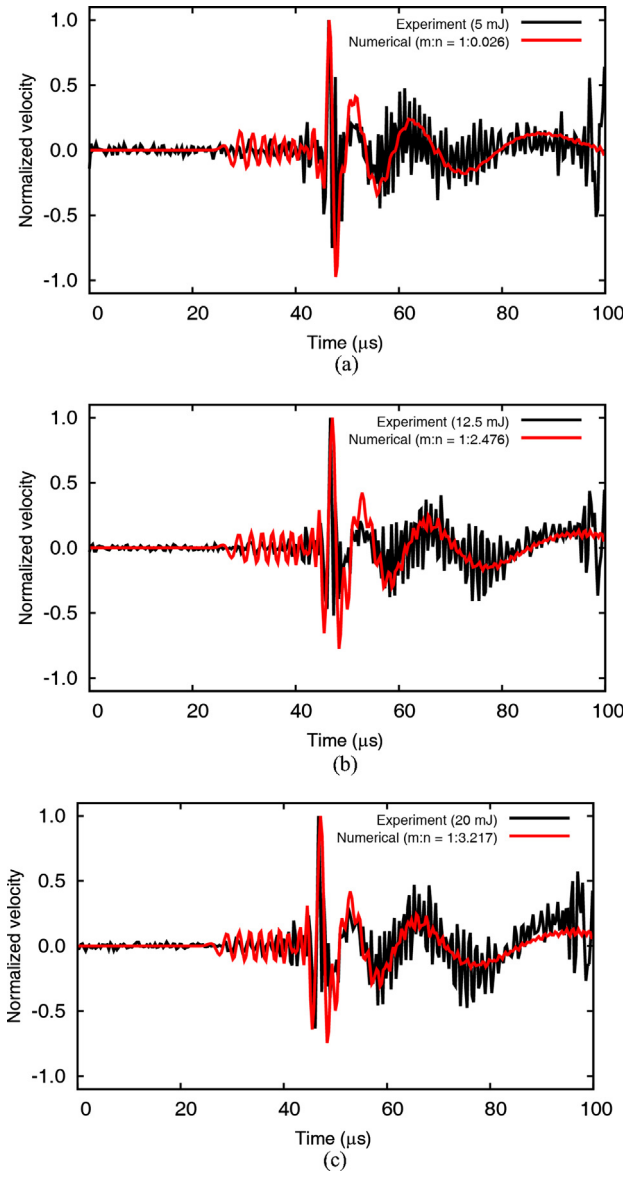

Fig. 10. Comparison of experiment results by mixing two waves generated by normal and radial tractions. The mixing ratio (m/n) of the two waves was determined using the least square method to minimize the error with the experiment results. The energy levels of the laser are (a) 5 mJ, (b) 12.5 mJ, and (c) 20 mJ, respectively.

method, we find the ratio of m and n that minimizes the difference between the experiment results and the synthesized numerical results. The synthesized waves found from the least square method are plotted in Fig. 10. In the experiment, ablation was observed at an energy level of 7.5 mJ. In Fig. 10(a), ablation was not observed with a laser level of 5 mJ. Fig. 10(b) and (c) shows the laser level of 12.5 mJ and 20 mJ, respectively. By the mixing ratios m and n of the numerical results, the effect of radiation pressure was increased compared to the result in Fig. 10(a). The effect increased as the energy level increased. The ratios of m and n to total energy are plotted in Fig. 11. If ablation did not occur, the proportion of the radiation pressure was negligible, but the ratio increased as the ablation takes place. The ratios converge with larger energy than 12 mJ.

At the intensity at which ablation does not occur, the laser-induced wave can be reproduced by considering only thermal expansion, but the radiation pressure must be considered if ablation occurs.

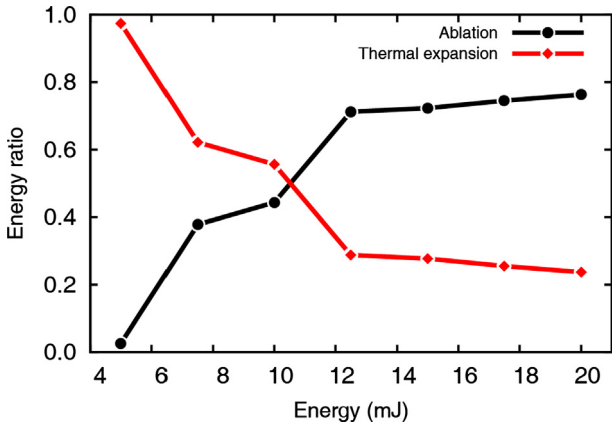

Fig. 11. The proportion of the heat flux and radiative pressure to the total energy. As the energy level increases, the contribution by the heat flux decreases and the contribution by the radiation pressure increases.

5. Summary and conclusions

In this study, we experimentally and numerically investigated waveforms generated by laser pulses. Experiments were carried out by changing the energy level of an ND: YAG pulse laser from 5 mJ to 20 mJ, while keeping the diameter the circular excitation area of 0.5 mm. In experiments, elastic waves were generated on an aluminum plate by changing the energy level. The velocities in the thickness direction were measured using a Laser Doppler Velocimeter (LDV) at a point 135 mm away from the excitation point. In the numerical study, a mesh modeling process was performed using a commercial program Hypermesh [22], and a numerical analysis was performed using a commercial FEM program, LS-Dyna. Two numerical simulations were carried out using heat flux and normal stress inputs to mimic laser pulse excitation. A thermo-mechanical simulation with heat flux was conducted to simulate thermal expansion, and normal stress was applied to reflect the effect of radiation pressure, respectively. The numerically obtained waveforms are utilized to synthesize the waveforms to match the experiment results. In this parametric study, the contribution ratios of those numerical results were inversely calculated.

It is found that the effects of thermal expansion and radiation pressure exist simultaneously if ablation takes place. Therefore, the effect of radiation pressure cannot be neglected when the energy intensity is large although the effect of radiation pressure decreases as the energy intensity decreases below a certain level. The investigation result would be beneficial to determine the appropriate energy intensity to maximize the signal to noise ratio of the experimental data while minimizing the unwanted mixture of the responses from the normal and radial tractions.

Acknowledgements

This work was supported by the National Research Foundation of Korea (NRF) Grant funded by the Korean Government (Ministry of Science and ICT) (No. 2017R1A5A1014883), and was also supported by a grant (13SCIPA01) from the Smart Civil Infrastructure Research Program funded by Ministry of Land, Infrastructure and Transport (MOLIT) of the Korean government and the Korea Agency for Infrastructure Technology Advancement (KAIA).

References

[1] P. Cawley, Non-destructive testing-current capabilities and future directions, Proc. Inst. Mech. Eng. Part L: J. Mater.: Des. Appl. (2001) 213–223.
[2] S.E. Lee, S. Jin, J.W. Hong, Periodic nonlinear waves resulting from the contact interaction of a crack, J. Appl. Phys. 122 (2017).
[3] H. Nakano, S. Nagai, Crack measurements by laser ultrasonic at high temperatures,

Jpn. J. Appl. Phys. 32 (1993) 2540–2542.
[4] J.L. Rose, Ultrasonic guided waves in structural health monitoring, Key Eng. Mater. 270–273 (2004) 14–21.
[5] J. Davies, P. Cawley, The application of synthetic focusing for imaging crack-like defects in pipelines using guided waves, IEEE Trans. Ultrason. Ferroelectr. Freq. Control. 56 (2009) 759–771.
[6] S.E. Burrows, B. Dutton, S. Dixon, Laser generation of Lamb waves for defect detection: experimental methods and finite element modeling, IEEE Trans. Ultrason. Ferroelectr. Freq. Control. 59 (2012) 82–89.
[7] R.J. Dewhurst, D.A. Hutchins, S.B. Palmer, C.B. Scruby, Quantitative measurements of laser-generated acoustic waveforms, J. Appl. Phys. 53 (1982) 4064–4071.
[8] J.D. Aussel, A. Le Brun, J.C. Baboux, Generating acoustic waves by laser: theoretical and experimental study of the emission source, Ultrasonics 26 (1988) 245–255.
[9] T.W. Murray, J.W. Wagner, Laser generation of acoustic waves in the ablative regime, J. Appl. Phys. 85 (1999) 2031–2040.
[10] Y. Guo, D. Yang, Y. Chang, W. Gao, Effect of oblique force source induced by laser ablation on ultrasonic generation, Opt. Express 22 (2014) 166–176.
[11] S.G. Pierce, B. Culshaw, W.R. Philp, F. Lecuyer, R. Farlow, Broadband Lamb wave measurements in aluminium and carbon/glass fibre reinforced composite materials using non-contacting laser generation and detection, Ultrasonics 35 (1997) 105–114.
[12] X. Li, C. Wang, H. Xiang, G. Zhang, Finite element simulation of ultrasonic guided waves generated by a pulsed laser in human skin, Instrum. Sci. Technol. 34 (2006) 711–725.
[13] W. Liao, D. Yang, W. Feng, Simulation of laser ultrasonic for confirming the initial time & location during the generation phase, Proc. SPIE (2010) 784301.
[14] H. Lee, J. Yang, H. Sohn, Baseline-free pipeline monitoring using optical fiber–guided laser ultrasonics, Struct. Heal. Monit. An Int. J. 11 (2012) 684–695.
[15] H. Lee, H.U. Lim, J.W. Hong, H. Sohn, Mechanical impedance measurement and damage detection using noncontact laser ultrasound, Opt. Lett. 39 (2014) 3130–3133.
[16] W. Liu, J.W. Hong, Modeling of three-dimensional Lamb wave propagation excited by laser pulses, Ultrasonics 55 (2015) 113–122.
[17] A. White, J.W. Hong, S. Hong, J. Choi, Parameter estimation for wavelet transformed ultrasonic signals, NDT E Int. 44 (2011) 32–40.
[18] Y. Shi, S. Wooh, M. Orwat, Laser-ultrasonic generation of Lamb waves in the reaction force range, Ultrasonics 41 (2003) 623–633.
[19] C.B. Scruby, L.E. Drain, Laser Ultrasonics: Techniques and Applications, CRC Press, 1990.
[20] H. Lee, Structural Health Monitoring of Pipelines in nuclear power plants using optical fiber guided laser ultrasound, KAIST, 2014.
[21] Livermore Software Technology Corporation, LS-DYNA Keyword User's Manual, vol. I, 2007, pp. 1–2206.
[22] Altair, HyperWorks for LS-DYNA, 2011, pp. 1–104.